NANO · MICRO small
www.small-journal.com

Revealing Intrinsic Functionalization, Structure, and Photo-Thermal Oxidation in Hexagonal Antimonene

*Marta Alcaraz, Michael Fickert, Christian Dolle, Mahesh Eledath Changarath, Juan F. Sánchez-Royo, Yolita M. Eggeler, and Gonzalo Abellán**

Antimonene is one of the more exciting members of the post-graphene family with promising applications in optoelectronics, energy storage and conversion, catalysis, sensing or biomedicine. Efforts have been focused on developing a large-scale production route, and indeed, through a colloidal approach, high-quality few-layers antimonene (FLA) hexagons have been recently obtained. However, their oxidation behavior remains unexplored, as well as their interface, inner structure, and photothermal properties. Herein, it is revealed that the hexagons have an intrinsic surface functionalization with alkyl thiols that protects the core of the hexagonal flake against oxidation, and displayed inner defects related to the crystal formation during synthesis, as confirmed by cross-sectional scanning transmission electron microscopy energy dispersive X-ray spectroscopy (STEM-EDX) and temperature-dependent X-ray photoelectron spectroscopy (XPS) and selected area electron diffraction (SAED) analysis. A comprehensive study of temperature and laser power-dependent Raman spectroscopy on varying FLA hexagon thicknesses is carried out. Thinner flakes (<20 nm) exhibited a blueshift and intensity decrease, contrasting with thicker ones resembling typical exfoliated flakes with a redshift. This work addresses a literature gap, providing insights into hexagonal FLA structure and characterization, and highlighting the influence of surface functional groups on oxidation behavior. Additionally, it emphasizes the potential of antimonene hexagons as building blocks for 2D heterostructures, including combinations with antimonene oxides and other 2D materials.

1. Introduction

Since the discovery of graphene in 2014, a new generation of 2D materials, including boron nitride (h-BN), transition metal dichalcogenides (TMD), and MXenes, have emerged.[1–4] Among others, monoelemental 2D materials such as 2D-Pnictogens (P, As, Sb, Bi) have attracted particular interest due to their exceptional and customizable physico-chemical properties, which have led to a wide range of applications in optoelectronics, energy storage and conversion, catalysis, sensing or biomedicine to name a few.[5–11] Antimonene, a monolayer of β-antimony, is of particular interest due to its rich structural allotropy, strong spin-orbit coupling, and semiconductor behavior (in the monolayer regime), which can be modulated by the number of layers, surface functionalization or physical stimuli, offering great versatility.[12,13]

Similar to other 2D materials, antimonene can be isolated using top-down or bottom-up approaches.[14] While top-down approaches such as micromechanical exfoliation[15] or liquid phase exfoliation[16,17] are commonly used methods, they face limitations in producing large and high-quality single or few-layer antimonene nanosheets. Bottom-up approaches such as molecular beam epitaxy[18] and van der Waals beam epitaxy[17,19] have demonstrated the ability to obtain high-quality antimonene, but they have not been successful in scaling up.[14] Recently, the wet-chemistry approach has been able to produce significant quantities of few-layer antimonene (FLA) with a hexagonal morphology, exhibiting lateral sizes up to several

M. Alcaraz, G. Abellán
Instituto de Ciencia Molecular (ICMol)
Universidad de Valencia
Paterna 46980, Spain
E-mail: gonzalo.abellan@uv.es

The ORCID identification number(s) for the author(s) of this article can be found under https://doi.org/10.1002/smll.202404319

DOI: 10.1002/smll.202404319

M. Fickert
Department of Chemistry and Pharmacy and Joint Institute of Advanced Materials and Processes (ZMP) Friedrich-Alexander-Universität Erlangen-Nürnberg (FAU)
90762 Fürth, Germany

C. Dolle, Y. M. Eggeler
Laboratory for Electron Microscopy (LEM)
Microscopy of Nanoscale Structures & Mechanisms (MNM)
Karlsruhe Institute of Technology (KIT)
76131 Karlsruhe, Germany

M. E. Changarath, J. F. Sánchez-Royo
UMDO, Instituto de Ciencia de los Materiales (ICMUV)
Universidad de Valencia
Paterna 46980, Spain

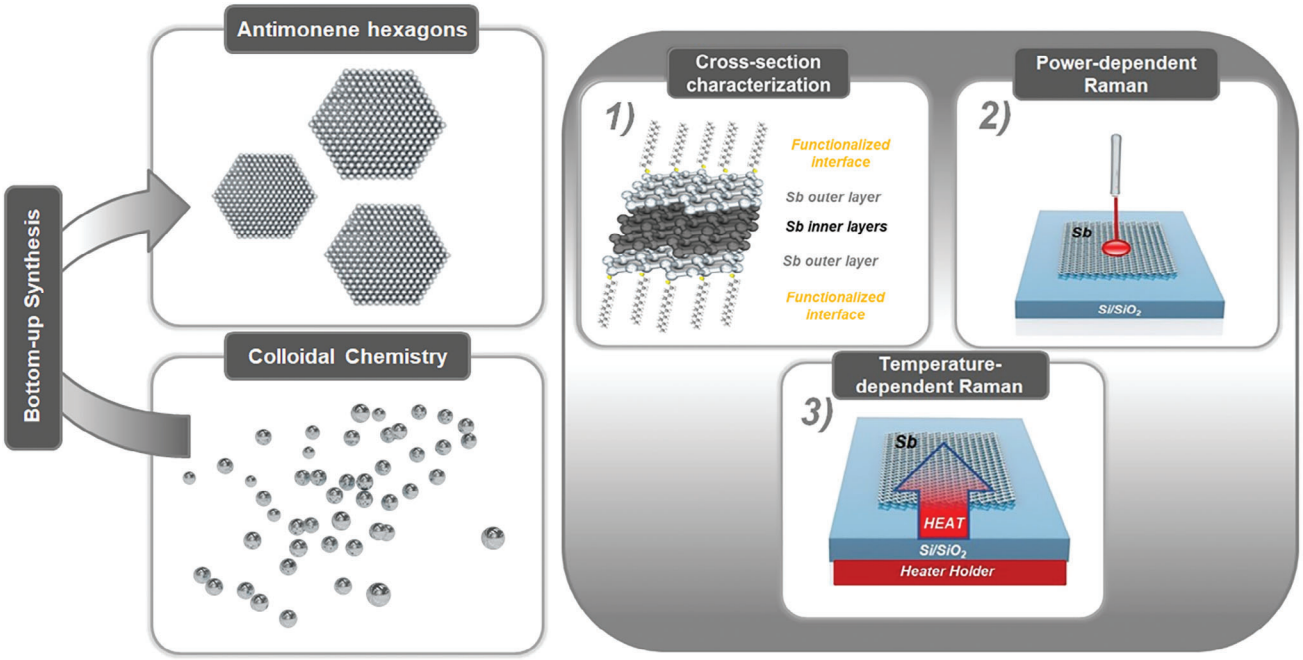

Scheme 1. Experimental approach summarizing the synthesis of antimonene hexagons through a bottom-up colloidal method. Subsequent analyses included 1) cross-sectional investigations using FIB-SEM and STEM-EDX, along with 2) laser power-dependent and 3) temperature-dependent Raman studies.

micrometers and thicknesses ranging from 5 to 30 nm, opening new avenues for scalability.[20] Antimonene possesses excellent stability under ambient conditions compared to its counterpart black phosphorous (BP), this is mainly due to the passivated antimony oxide layer present on the surface.[21] The oxidation of antimonene nanosheets may take place during the obtention process, such as in the liquid-phase exfoliation process[22] especially when employing polar solvent mixtures like isopropanol/water, unless stringent inert conditions are employed.[8] We have recently investigated the effect of temperature and laser irradiation in the oxidation behavior of LPE and micromechanically exfoliated antimonene, showing a change in the surface electronic properties upon oxidation. Specifically, a surface 2D antimony oxide –which is stoichiometry-dependent– is generated, exhibiting different structural stability and electronic properties, ranging from topological insulators to semiconductors with direct and indirect bandgaps between 2.0 and 4.9 eV.[23,24] However, the oxidation behavior and the effect of temperature or laser irradiation on the novel antimonene hexagons remain unexplored, precluding their use in novel applications. Moreover, the presence of linked thiols on the surface of these hexagons, which in the case of bismuthene has shown to provide good resistance to oxidation,[25] remains an open question. This is mainly due to very labile bonds, the presence of surface residuals, as well as noticeable amount of oxygen located at the surface and edges of the nanosheet.[20]

Herein we investigate the structure of FLA hexagons obtained via wet chemistry involving surfactants and thiol species. Using focused ion beam scanning electron microscopy (FIB-SEM) and scanning transmission electron microscopy coupled with energy dispersive X-ray spectroscopy (STEM-EDX) we managed to decipher the internal structure of the nanosheets as well as the presence of a sulfur-encapsulation layer on both sides of the crystallites. In addition, the obtained hexagons exhibit structural defects caused by the experimental conditions during the synthesis. Furthermore, for the first time, the oxidation of FLA hexagons of different heights was studied using temperature and laser power-dependent Raman spectroscopy, atomic force microscopy (AFM) and temperature-dependent X-ray photoelectron spectroscopy (XPS). The findings facilitate a comparison of the thermal oxidation stability of antimonene hexagons, ranging in thickness from 10 to >20 nm, obtained through both top-down and bottom-up approaches, showing that the presence of surface thiols provides a protection against surface oxidation.

2. Results and Discussion

2.1. HAADF-STEM Measurements

The hexagonal antimonene nanosheets were synthesized using a wet-chemistry procedure previously reported[26] by Peng and coworkers and optimized by our group[20] yielding a well-defined structure and hexagonal morphology with measured heights of ≈10.5 nm and lateral dimensions of ≈2 µm (**Scheme 1**).[20] In order to describe the internal microstructure of the FLA hexagon, we extracted a cross-sectional FIB lamella. The selected flake had a thickness of 20 nm with a diameter of almost one micrometer, as can be seen in the high-angle annular dark field high-resolution and scanning transmission electron microscopy (HAADF-HRSTEM) images of **Figure 1**a. A protective Pt-layer was deposited using electron-beam and ion beam-induced deposition (EBID, IBID) in the FIB before the preparation of the

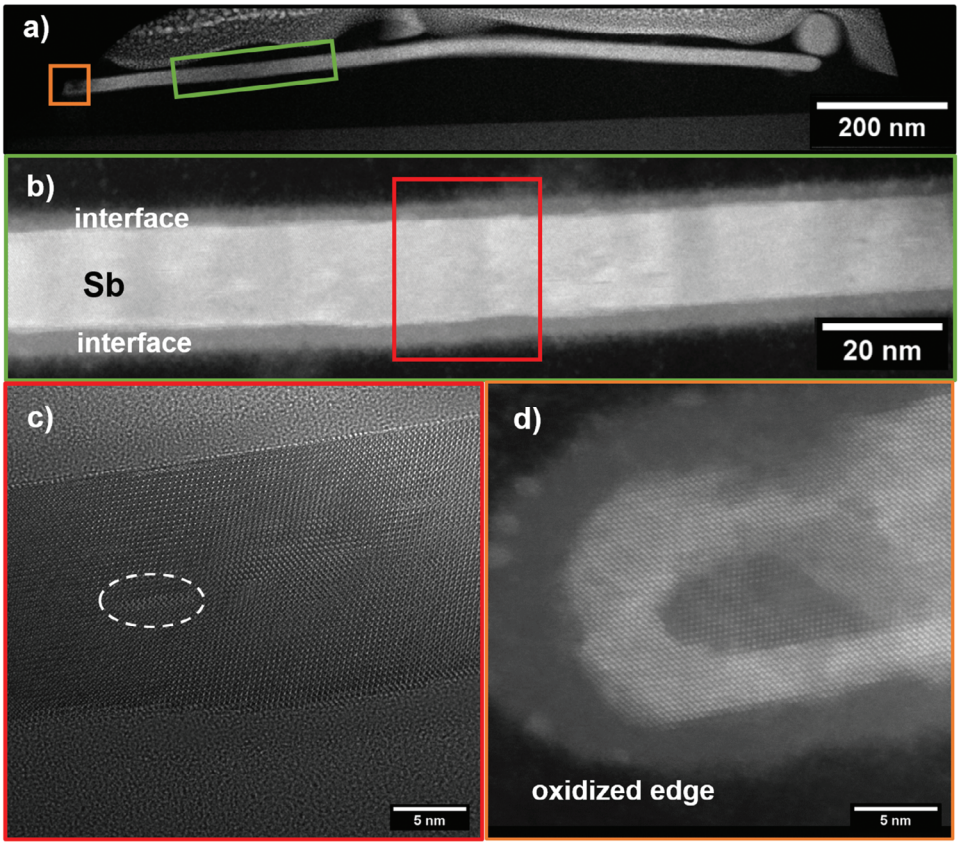

Figure 1. Cross-section preparation of FLA hexagons. a) STEM image after deposition of protective Pt layer. b) HAADF-STEM focus image of the interfaces of antimonene with the green square in a. c) HRTEM image of the internal defects in the lamella highlighted with the red square in (b). Selected defective area has been highlighted with a white circle for clarity. d) HAADF-STEM focus image of the oxidized edge with the orange square in (a) of the antimonene flake during the analysis.

cross-section to protect the interface of the FLA flake. This is a matter of utmost importance for protecting the integrity of the pristine surfaces. In addition, as can be seen in Figure 1b, which is a zoom of the green part in Figure 1a, the FLA hexagon is located between two amorphous layers of a few nanometers. Although the interfaces exist from the beginning of the cross-section FIB lamella, Figure 1d shows the edge of the flake that underwent oxidation during electron beam focusing, highlighting the surface chemical reactivity of antimonene.

In the enlarged Figure 1c can be clearly seen that the antimonene flake exhibits local defects in the atomic structure, and these defects are also observed in the spherical-shaped antimony nanoparticle depicted in Figure S1c (Supporting Information). Taking into account the contrast of the image in Figure 1c and Figure S1b (Supporting Information), these defects show signs of internal deviation of the rhombohedral stacking from ABC and thus represent in-grown stacking faults, rather than vacancy defects such as multi vacancies, as observed in BP.[27] On the one hand, other intrinsic defects, such as Stone-Wales defects could be formed during the nucleation and growth stages in the colloidal synthesis of the nanosheets. However, Stone-Wales defects require a change in the connectivity of two atoms via the rotation of a bond. Each Stone-Wales defect provokes the formation of two new bonds through 90°. Nevertheless, these kinds of defects are usually located at specific points in the structure, not along the crystal in the xy plane.[28,29] On the other hand, it is known that β-antimonene can be stacked following different patterns: ABC or AAA stackings,[30] with ABC stacking being the most stable form. The colloidal synthesis of FLA hexagons involves high temperatures, which might promote the locally constraint re-stacking of the rhombohedral ABC form into AAA and thus the introduction of stacking faults.[31] As a result, we suggest the experimental conditions can help in the formation of a new stacking in certain areas in the core of the FLA hexagon. It is worth to mention that the lateral elongation of these planar defects is highly homogenous and consists of only a few unit cells with a lateral dimension of ≈5 nm. Interestingly, these defects have not been observed in few-layer bismuthene prepared by a colloidal synthesis and characterized using a similar experimental approach.[25]

In order to elucidate whether the interface of this hexagonal antimonene contains thiols or not, STEM-EDX mappings were recorded from the prepared cross-section. **Figure 2** shows a closer elemental examination of the observed amorphous interface of a FLA hexagon and the overall constitution of the crystallite. The STEM-EDX mappings show the distribution of antimony, sulfur, and oxygen along the cross-section lamella of the FLA hexagon. The sulfur distribution map reveals that the encapsulation layer contains sulfur. The sulfur species are localized directly at the

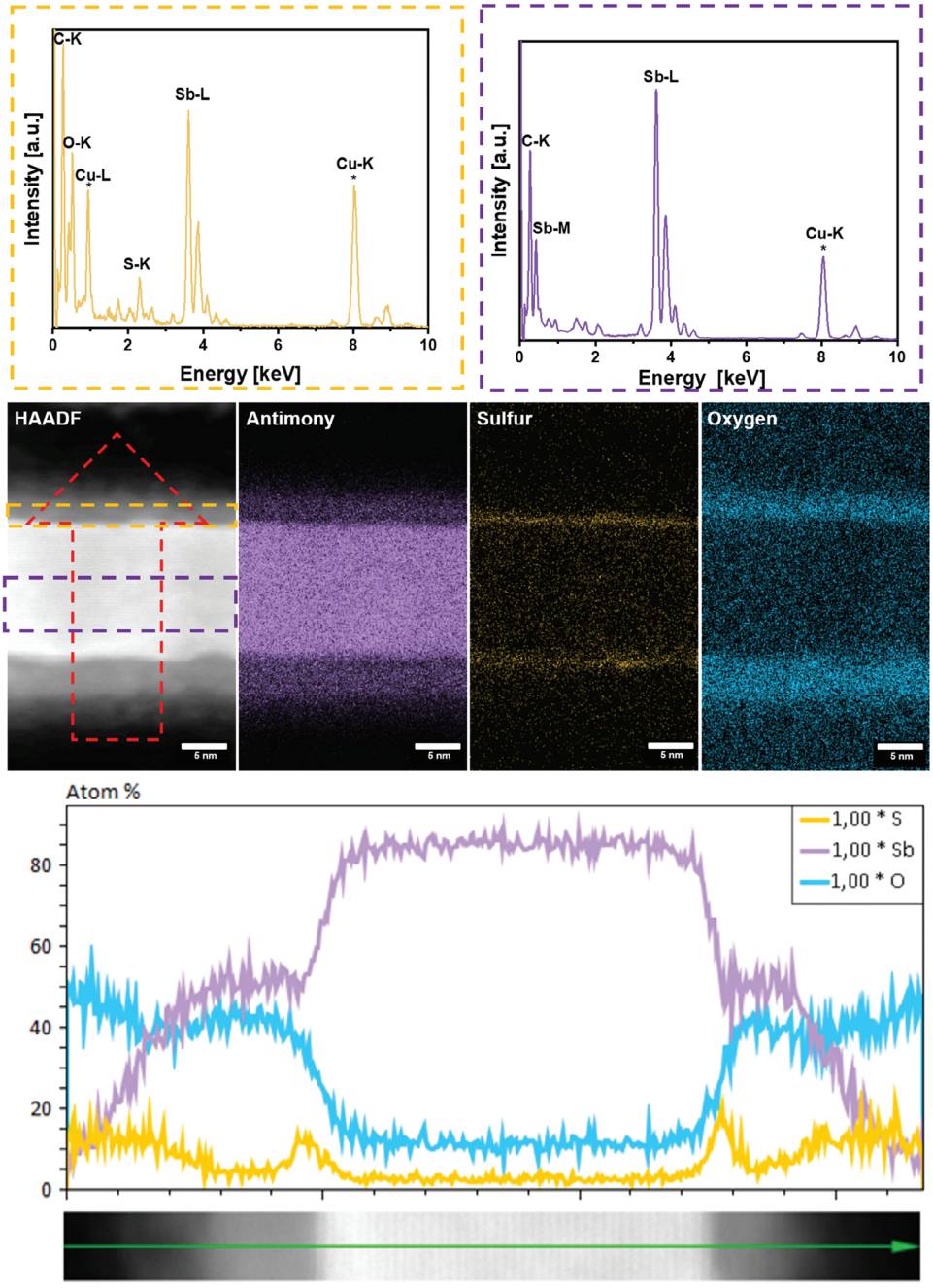

Figure 2. Cross sectional STEM-EDX mapping of a FLA hexagon. Line scan evaluation of normalized mass percentage for Sb, S, and O signal. Line scan extracted at the indicated position shown in HAADF-STEM image.

outer surface of the flake and are not contained within the material. This suggests the interface layer of FLA hexagon is covalently functionalized with sulfur species. From the oxygen distribution maps, can be assured there is no measurable oxidation inside the encapsulated layer, but away from the FLA internal surfaces. This means that the sulfur-functionalized layer is protecting the material against oxidation. The intensities of the Sb—L, S—K, and O—K peaks related to the encapsulation and inner antimonene flake are in concordance with the results extracted from the EDX mappings. The remaining oxygen visible in the presented line scans can be attributed to adsorbed oxygen species caused by the handling time between the preparation of the cross-sectional lamella and the final measurement of the EDX mapping. It cannot be avoided, even for sample storage in an inert gas glove box in between the experiments, as pure antimony is highly prone to oxidative saturation of its free interfaces upon exposure to ambient conditions. Now that we have elucidated the internal structure of the antimonene hexagons, we are in a good position to investigate the influence of laser power on the oxidation behavior, as well as the protective role played by surface thiols.

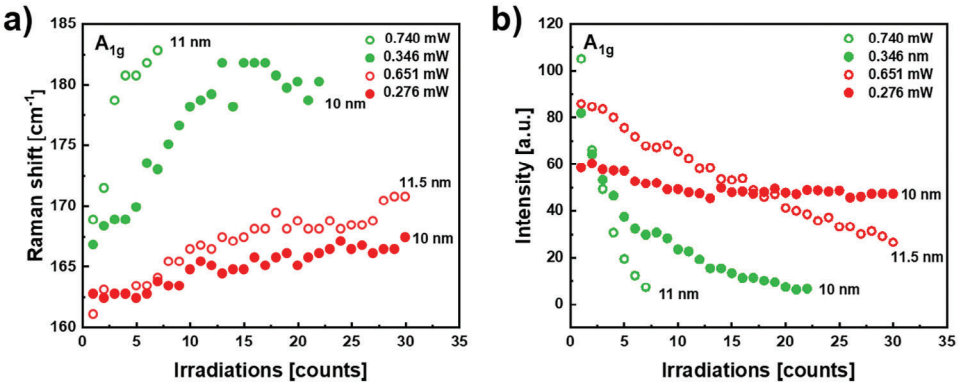

Figure 3. Laser-power dependent Raman spectroscopy. Measurements of four thin (10–11.5 nm) FLA hexagons using laser wavelengths of 532 nm (green scattered lines) and 633 nm (red scattered lines) with different laser powers and 1s acquisition time. a) Raman shift evolution of the A_{1g} mode of the FLA hexagons shown in Figures S2 and S3 (Supporting Information) using different wavelengths and laser powers. b) Course of the Raman intensity of A_{1g} of FLA hexagons shown in Figures S2 and S3 (Supporting Information) using different wavelengths and laser powers.

Laser irradiation has a big influence on the optical behavior and thermal properties of micromechanically exfoliated antimonene nanosheets, inducing the formation of surface oxides. In this line, a detailed analysis employing different laser powers was carried out using antimonene hexagons of ≈10 nm thickness.[23] In **Figure 3** we present the Raman measurements of four selected FLA hexagons with similar thickness (Figures S2 and S3, Supporting Information), and their corresponding evolution of the Raman shift and intensity of the A_{1g} vibrational mode. Thereby, repeated measurements of one second acquisition time were conducted with the same laser energy to evaluate only the effect of constant laser power on the material. These types of measurements are relevant in the context of the standard characterization of antimonene flakes. Using 532 nm with a power of 0.740 mW, the repeated power-dependent Raman experiments of the FLA hexagon shown in Figure S2 (Supporting Information) a and b were measured. Both, A_{1g} and the E_g signals decreased and blueshift, until the eighth measurement. After that, no signal was measurable anymore. Figure 3a shows how the Raman shift of A_{1g} increases with a power of 0.740 mW. At the beginning, A_{1g} shifts slightly. However, at the third measurement, a huge shift of 7 cm^{-1} can be observed. Afterward, only a minimal shift can be observed. Similarly, the intensity of the A_{1g} peak decreased sharply from the beginning (Figure 3b), but the decrease becomes less obvious with each measurement until no signal remains. This fact already demonstrates that no external heat is needed to induce the shift, hence oxidation, in the FLA nanosheets. Since the laser's effect is noticeable up to the eighth measurement, using a lower laser power could enhance the precision of the observed transformation. Hence, a laser power of 0.346 mW was used to repeat the experiment in a different FLA hexagon (Figure S2c,d, Supporting Information). Thereby, Figure 3a highlights the same blueshift without external heat. At first, the intensity of the A_{1g} peak (Figure 3b) decreases constantly, whereby the decrease becomes less remarkable with each dose reaching a minimum after >20 irradiation steps. If the energy used becomes lower, almost no antimony signal can be detected as the excitation intensity is too low.

The previous experiment (Figure 3) using a laser wavelength of 532 nm shows that laser power plays a very important role in the interface oxidation. The energy transferred to a sample by a laser depends on the absorption of the material, so the material should behave differently when a different wavelength is used. Hence, the same experiment was performed using a laser wavelength of 633 nm and a laser power of 0.651 mW in the FLA hexagon of Figure S3b (Supporting Information). The blueshift and the decrease of the intensity of the A_{1g} peak were still observable (Figure S3a, Supporting Information), and even after 30 measurements the A_{1g} and the E_g signals of antimony are still present. Figure 3a shows the signal blueshifts constantly until the 15th measurement is reached. Therefore, this shift remains at ≈168 cm^{-1} until the 27th measurement. On the other hand, the intensity of the A_{1g} (Figure 3b) decreases until the end of the experiment. Also, with a power of 0.651 mW of the red laser, it is possible to measure more often without causing a complete surface modification, with no significant Sb_2O_3 signals at ≈190.5 and 254.6 cm^{-1}. With this in mind, we use the 633 nm laser and a lower laser power of 0.276 mW from now on (Figure S3c,d, Supporting Information). Figure 3a shows that the Raman signal shifts gradually from 162.5 cm^{-1} to 167.5 cm^{-1}. Additionally, the intensity decreases until the 10th measurement, whereon it remains nearly constant and only a very small decrease can be detected (Figure 3b). Although the transformation cannot be avoided by using a red laser, it considerably slowed down. Overall, 633 nm is a more promising laser than 532 nm to minimize changes in the material.

To further investigate the surface transformations in FLA hexagons, temperature-dependent Raman measurements of nanosheets with different thicknesses have been carried out. The laser chosen is 633 nm to analyze the transformation in more detail, with a power of 0.651 mW (instead of 0.276 mW) as the used Linkam heating chamber (THMS 600) reduces the received signal. The experiment is conducted under a nitrogen flow, but the holder is not completely hermetic; therefore, oxygen is present during the experiments.

The hexagon that was measured had a thickness of 10.3 nm (**Figure 4c**) and showed a purple color at the beginning, indicative of a low thickness. The temperature was increased from room temperature to 100 °C, following 10 °C steps. At the beginning, the pristine antimonene presents the A_{1g} and

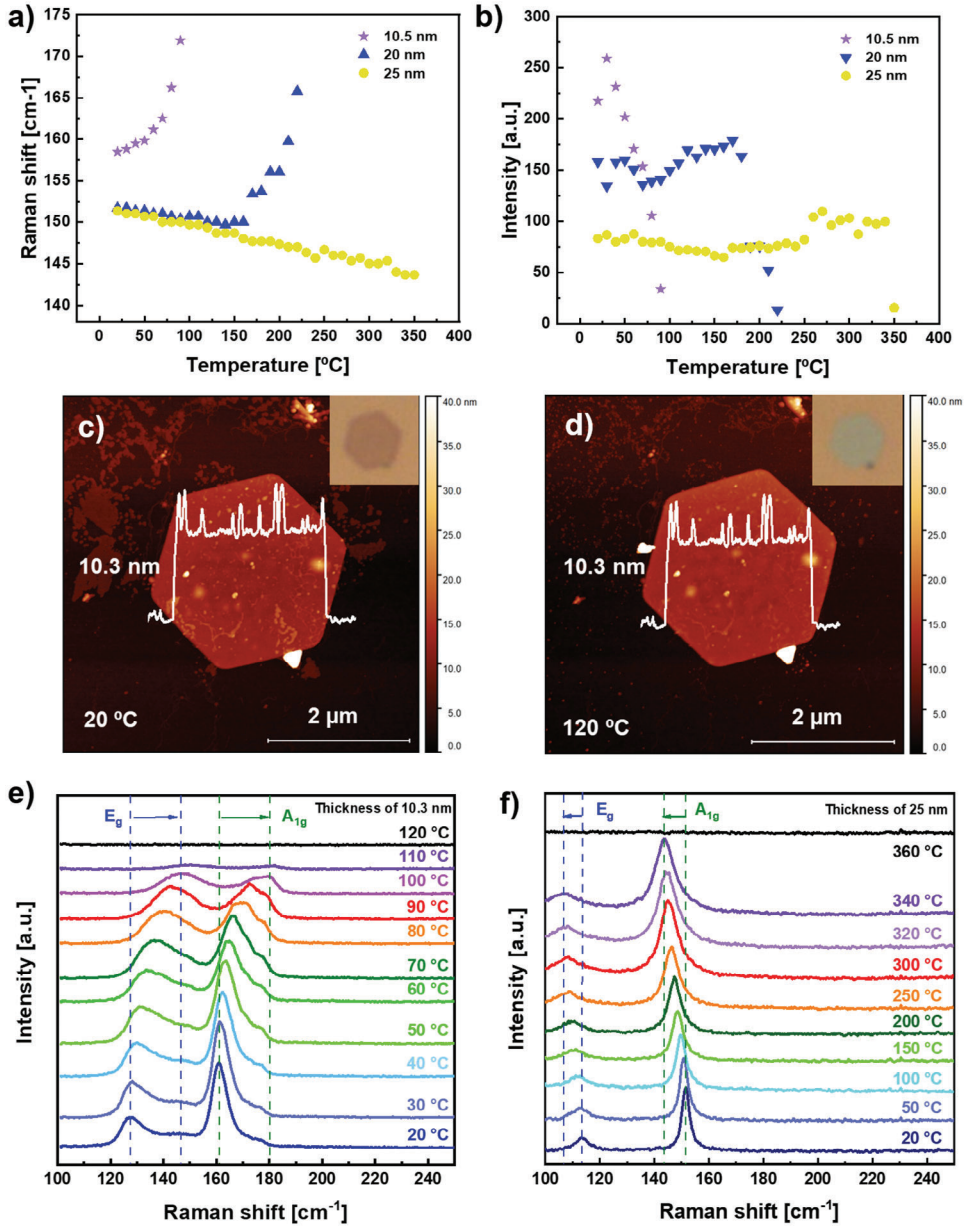

Figure 4. Temperature-dependent Raman spectroscopy. a) Correlation between the Raman shift of A_{1g} and the temperature for three FLA hexagons of 10, 20, and 25 nm thickness using a laser wavelength of 633 nm with 1s acquisition time. b) Thermal evolution of the A_{1g} Raman mode intensity of the FLA hexagons presented in Figures S5, S7, and S8 (Supporting Information). c) AFM image of a 10.3 nm thick FLA hexagon before laser irradiation at 20 °C. d) AFM image of the same hexagon after laser irradiation at 120 °C. The insets show the corresponding optical images. e) Temperature-dependent Raman measurements of a 10.3 nm FLA hexagon ranging from room temperature (20 °C) to 120 °C. f) Temperature-dependent Raman measurements of a 25 nm FLA hexagon ranging from 20 to 360 °C.

the E_g signals at ≈160 and ≈127 cm^{-1}. Upon heating the Raman signal of A_{1g} blueshifts marginally with each measurement (Figure 4e; Figure S4, Supporting Information), but after reaching 70 °C the shift becomes more pronounced, as highlighted in Figure 4e. Regarding the intensity, it decreases rapidly until 120 °C, where no signal can be detected anymore. Normally, the decrease in the intensity of the Raman modes is attributed to the decomposition of the nanomaterial which, however, is not the case here. Although no signal was found after the last measurement, the FLA nanosheet remained with a blue color after the measurements as shown in Figure 4d. The temperature-dependent Raman of an additional FLA hexagon was measured (Figure S5, Supporting Information) showing the same change in the color from purple to light blue and Raman shift tendency (Figure 4a). In addition, it was observed in Figure 4d that the antimonene hexagon after the experiment exhibited the same thickness, in contrast to micromechanically exfoliated flakes previously reported.[23] This experiment suggests that

the optical change only takes place in the thinner antimonene hexagons.

In order to confirm that no decomposition was occurred, we carried out a temperature-dependent Raman with a heating/cooling ramp of 10 °C min^{-1} of two similar FLA hexagons using both lasers, 532 and 633 nm (Figure S6a,b, Supporting Information). According to Figure S6a (Supporting Information), the selected antimonene flake irradiated with the laser 532 nm (Figure S6a, Supporting Information), presents the A_{1g} and the E_g signals at ≈160 and ≈123 cm^{-1}. The blueshift of both A_{1g} and E_g modes is clearly observed as the temperature of the sample increases. Moreover, the intensities of the signals decrease with no signal left at 100 °C. The faster the temperature increases, the faster both Raman modes disappear. After the holder raised 100 °C, we cooled it and the intensity of both vibrational modes recovered again with a permanent shift to higher wavenumbers. Along this front, another experiment was carried out using a similar nanosheet and 633 nm laser (Figure S6b, Supporting Information). The selected flake presents the A_{1g} and the E_g signals at ≈161 and ≈127 cm^{-1}. Increasing the temperature, it could be observed the same behavior as irradiating with the laser 532 nm (Figure S6a, Supporting Information), but the peaks disappeared after reaching 200 °C. Again, the color of the flake changed from purple to light blue after the heating experiment with no observable decomposition of the material. This light blue color was maintained during the cooling experiment (Figure S6d,e, Supporting Information). Finally, at 100 °C it was possible to detect the peaks of both vibrational modes again with slight blueshifts. All these modifications are ascribed to the formation of a 2D oxide surface passivation layer, which does not affect the whole hexagon. Due to the anharmonic vibrations of the altered lattice and its expansion at highest temperatures in the experiments, the interatomic forces change constantly.[32–34] As a consequence, it cannot be possible to detect antimony signals by Raman anymore. After cooling, the antimonene structure relaxed to its equilibrium positions, resulting in signal recovery with lower intensity and a notable color change tentatively associated with the formation of a 2D surface antimony oxide layer. This behavior may account for the previously reported Raman attenuation in LPE Sb layers with thicknesses below 30 nm, indicating significant oxidation.[15]

In order to determine whether this behavior is dependent on the thickness of the sample, we have conducted similar experiments with nanosheets of different thicknesses. A FLA nanosheet with a thickness of 20 nm has been selected (Figure S7, Supporting Information), showing a yellow metallic shimmer similar to bulk antimony (Figure S7a, Supporting Information). Due to its yellow color and its height, we expect a similar behavior as bulk antimony, which was only partially the case. At the beginning of the heating experiment (Figure 4a), the Raman signal of A_{1g} redshifts similar to bulk antimony, but at 180 °C a change occurs (Figure 4a; Figure S7c, Supporting Information). The signal starts to blueshift, which does not change until the end of the measurement. The beginning can be attributed to the thermal expansion of the material, whereas the blueshift is similar to the behavior of the FLA nanosheets. Furthermore, the intensity of the A_{1g} peak shows the same trend (Figure 4b). At the beginning of the experiment, the intensity behaves similarly to bulk antimony and it remains more or less constant, but at ≈ 180 °C the intensity dramatically drops until no signal is left at 230 °C. At the end of the experiment, an optical image was taken. As can be seen in Figure S7b (Supporting Information), the color of the FLA nanosheet changed to light blue, so no decomposition of the material was observable in the area where the transformation occurred. The light blue color is attributed to the formation of 2D oxidized layer as previously indicated.[15,35]

Furthermore, to gain information of thicker bulk-like FLA hexagons, samples with 25 nm thickness were measured (Figure 4f; Figure S9, Supporting Information). Before the experiment, the selected nanosheets manifested a yellow metallic shimmer of bulk antimony (Figure S8a, Supporting Information). In this case, the hexagons exhibited an evident redshift of both A_{1g} and E_g peaks, as the temperature increases (Figure 4a). From the beginning of the measurements at 20 °C until the end at 350 °C, a constant redshift of the Raman signal was visible (Figure 4f; Figure S9d, Supporting Information). Such a redshift is always expected when the material is heated up due to a lattice expansion. Moreover, the intensity stayed constant until 250 °C (Figure 4b), whereupon an intensity increase could be observed, which is most likely attributed to the oxidation of the material. Afterward, the signal decreased rapidly until no signal remained after 350 °C. In that case, the FLA nanosheet decomposed and the flake vanished after the experiment, as can be seen in Figures S8b and S9c (Supporting Information). This behavior is dramatically different compared to thinner antimony nanosheets and similar to that of micromechanically exfoliated flakes and bulk antimony.[23,36] These experiments evidence that FLA hexagons of >20 nm thickness behave as bulk antimony.[23]

Finally, for comparative purposes, we carried out the same procedure using micromechanically exfoliated antimonene flakes with thicknesses ranging between 18–23 nm (Figure S10a,c, Supporting Information).[23] The analyzed polygonal flakes had a yellow metallic luster characteristic of bulk antimony.[11] The mean Raman spectra extracted from Raman mapping in Figure S11 (Supporting Information) depict the selected Raman area at 20 and 280 °C (Figure S10e,f, Supporting Information). At the beginning of the temperature-dependent Raman experiment, no noticeable changes were observed. (Figure S10e, Supporting Information). The Raman map at 280 °C (Figure S11, Supporting Information) depicts the signal of the bigger flakes at the top and the bottom of the map, respectively. The intensity of the thinner flakes is lower but it still remains at 280 °C (Figure S10f, Supporting Information). Furthermore, an obvious color change from yellow to blue can be seen in the optical image after the measurement (Figure S10b, Supporting Information). Interestingly, an increase in the thickness of ≈1.5 nm can be observed after the measurements in the AFM image of Figure S10d (Supporting Information). This behavior, which differs from that observed for the hexagons, is attributed to oxidation. Thin flakes tend to oxidize much faster than the bigger ones because they are more reactive.[11,37] In addition, an amorphous oxide film could form with little or no Raman signal, which is related to the increase in height.[23] These results pinpoint the protective influence of thiol functionalization on the oxidation behavior of antimonene hexagons.

To elucidate whether the oxidation is taking place and to extract precise data about its evolution during the thermal process

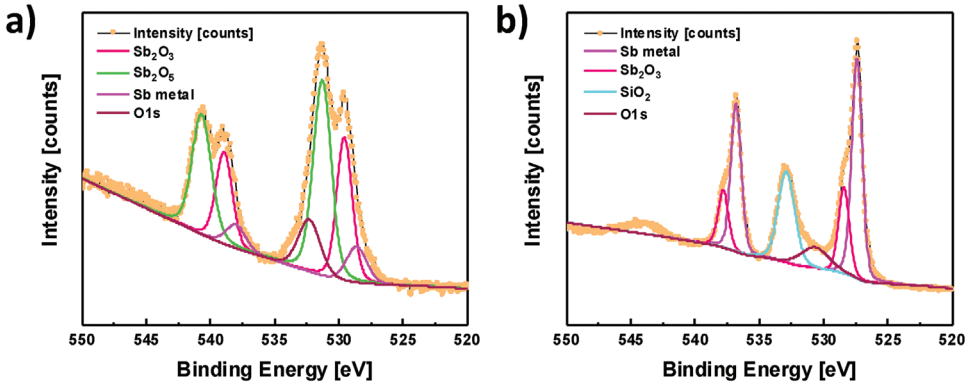

Figure 5. Surface characterization of FLA hexagons by high-resolution XPS. a) Sb 3d region measured at 25 °C and 1.0×10^{-10} mbar. b) Sb 3d region after annealing at 150 °C.

under strictly inert conditions, we have performed a series of XPS measurements using inert chambers measuring the samples before and after heating at 150 °C in ultrahigh vacuum conditions (base pressure of 1.0×10^{-10} mbar). **Figures 5** and S12 (Supporting Information) shows the Sb 3d core-level and survey spectra measured by XPS in a FLA hexagons sample prepared on a SiO_2/Si substrate. The spectra were deconvoluted by assuming Voigt line shape peaks and Shirley backgrounds, by considering Sb 3d doublets with a spin-orbit splitting of 9.4 eV. The deconvolution process revealed that the Sb 3d spectra of the as-received sample was composed by three doublets whose Sb $3d_{5/2}$ components appear at binding energies of 528.6, 529.6, and 531.3 eV, which are attributable to the presence of metallic Sb, Sb_2O_3, and Sb_2O_5 respectively.[20] Additional signal located at 532.3 eV is attributable to the O 1s. From the relative intensity ratio of the Sb-related XPS doublets resolved, it appears that the hexagons, after reaching the vacuum, exhibited an oxidized surface, as expected from the EDX data collected in Figure 2. These results contrast with the Sb 3d spectra measured in the sample annealed at 150 °C, in which signal from metallic Sb dominates over a smaller contribution coming from Sb_2O_3, presumably 2D antimony oxide (*vide infra*), whereas signal from Sb_2O_5 becomes no longer detectable. Moreover, no signal of sulphur was detected, suggesting that the thiols did not survive the annealing process under ultrahigh vacuum. These results indicate that annealing in vacuum strongly removes oxidated Sb-species observed on the surface of the hexagons leaving behind a subnanometric oxidation layer (Figures 1 and 2), as also suggests the observation of the Sb plasmon appearing at 544 eV, being indicative of a high-quality surface, although the detection of signal from the O 1s core-level coming from the SiO_2 substrate indicates that annealing reduces surface coverage.

Last but not least, to confirm our hypothesis, we conducted temperature-dependent selected area electron diffraction (SAED) on FLA hexagon with a thickness of ≈20 nm, ranging from 20 to 200 °C. **Figure 6** shows the expected hexagonal diffraction pattern of the beta phase viewed along the [001] zone axis, indicating that the FLA hexagonal crystal at 20 °C belongs to a rhombohedral structure. During the heating process, additional reflections appeared, corresponding to observed stacking faults (internal defects) that locally altered the stacking order of the crystal and thus gave rise to otherwise forbidden reflections in a purely rhombohedral crystal system. Furthermore, the functionalization of the FLA hexagons interfaces with the observed sulfur species can influence the resulting diffraction signal, as has been recently reported for bismuthene hexagons obtained via colloidal chemistry.[25] In addition, we cannot discard the presence of superficial oxidation in line with the STEM-EDX, the XPS experiments and the previous reports.[8,20] The absence of clear signals of oxidation in the SAED patterns as well as the results from temperature-dependent Raman and XPS spectroscopy (Figures S6 and S7, Supporting Information), confirms the protective role of surface functionalization with thiols against oxidation. Density functional theory (DFT) calculations of 2D antimony oxides[21] suggest that with enough energy, oxygen in the outer layers inserts into Sb–Sb bonds, forming Sb—O—Sb bonds. Indeed,

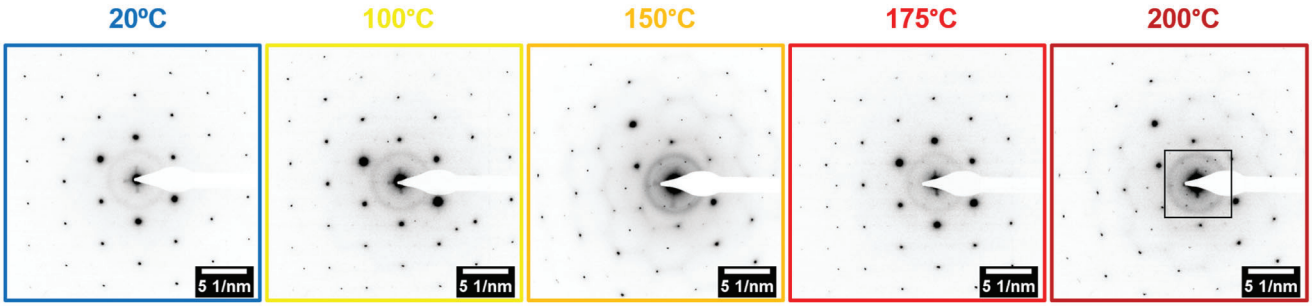

Figure 6. Temperature-dependent SAED pattern of a FLA hexagon. Starting at room temperature (25 °C) until 200° C.

by increasing the temperature, the oxygen present in the outer layers of conventional antimonene will be inserted in the Sb—Sb bonds, easily forming Sb—O—Sb bonds, in excellent agreement with T-dependent XPS data (Figure 5). This affects the inner, non-oxidized antimonene layers, modifying lattice parameters, and potentially Raman peak positions, as observed in defective and doped graphene.[38–40] Following this rationale, continuous lattice vibrations during temperature-dependent Raman revealed three effects: i) relaxation of distorted forces caused by oxygen insertion in the outer antimonene layer, ii) changes in color (to light blue), Raman peak positions, and (lower) intensities due to this insertion, and iii) challenges in detecting the Raman signal at high temperatures due to continuous structural vibration. These effects are more prominent in thinner flakes and can be minimized by the surface functionalization in FLA hexagons.

3. Conclusion

In conclusion, novel insights into the FLA hexagon structure were gained with STEM-EDX confirming intrinsic functionalization that safeguards the hexagons against oxidation. The as-synthesized antimonene hexagons also displayed defects linked to crystal formation and growth during colloidal synthesis. Moreover, we presented the first comprehensive study of the temperature-dependent and laser power-dependent Raman spectroscopy of FLA hexagons of different thicknesses. The observed blueshift to higher wavenumbers and substantial intensity decrease in the Raman signals of the thinner (<20 nm thick) FLA flakes changes for thicker ones, behaving like a typical micromechanically exfoliated one with the characteristic redshift. Optical and AFM images confirmed that the FLA hexagons did not decompose, but there was a change in the color of the materials from purple to light blue. This change in optical properties after Raman measurements (i.e., temperature and laser irradiation) is attributed to the formation of a semiconducting ultra-thin amorphous 2D antimony oxide layer that could not be detected by Raman, as confirmed by T-dependent XPS under ultrahigh vacuum.

In addition, as the number of layers increased, FLA hexagons exhibited bulk-like behavior similar to that observed for micromechanically exfoliated flakes with similar thicknesses. The synthesis of antimony nanosheets with controlled morphology and thickness –further featuring a surface functionalized with thiols for protection against uncontrolled oxidation– represents a novel avenue for the development of heterostructures based on antimony oxides/antimony, as well as combinations with other 2D materials.

This work fills a gap in the literature by providing insights into the structure of antimonene hexagons and deciphering the presence of surface functional groups, along with their influence on oxidation behavior. The findings reveal a promising strategy for controlling oxidation in antimonene nanomaterials, although these findings are not only restricted to their potential applications of these nanomaterials. From a fundamental point of view, these results also open the door to exploring the effects of quantum confinement on the electronic properties of bare FLA and their allotropes.

Supporting Information

Supporting Information is available from the Wiley Online Library or from the author.

Acknowledgements

M.A., M.F., and C.D. contributed equally to this work. This work was supported by the European Research Council (ERC Starting Grant No. 2D- PnictoChem 804110 and ERC Proof of Concept Grant 2D4H2 No. 101101079). This research was also financed by Grants PID2022-143297NB-I00, MRR/PDC2022-133997I00, TED2021-131347B-I00 and Unit of Excellence "Maria de Maeztu" CEX2019-000919-M funded by MCIN/AEI/10.13039/501100011033 and by ERDF/EU, and the Generalitat Valenciana (CIDEGENT/2018/001). The present work has been supported by the projects MFA 2022/009 (SPINO2D) and PROMETEO/2021/082 (ENIGMA) of the Generalitat Valenciana and the PID2020-112507GB-I00 project of the Ministerio de Ciencia e Innovacion. M.E.C. acknowledges financial support from the Santiago Grisolía Program of the Generalitat Valenciana (grant CIGRIS/2021/150). C.D. and Y.M.E. thank the cluster of excellence 3DMM2O funded by DFG under Germany's Excellence Strategy – 2082/1 – 390761711 for financial support.

Conflict of Interest

The authors declare no conflict of interest.

Data Availability Statement

The data that support the findings of this study are available from the corresponding author upon reasonable request.

Keywords

2D Pnictogens, antimonene, functionalization, oxidation, photo-thermal properties

Received: May 28, 2024
Revised: September 3, 2024
Published online:

[1] Y. Kubota, K. Watanabe, O. Tsuda, T. Taniguchi, *Science* **2007**, *317*, 932.
[2] S. Manzeli, D. Ovchinnikov, D. Pasquier, O. V. Yazyev, A. Kis, *Nat. Rev. Mater.* **2017**, *2*, 17033.
[3] A. VahidMohammadi, J. Rosen, Y. Gogotsi, *Science* **2021**, *372*, eabf1581.
[4] A. J. Mannix, B. Kiraly, M. C. Hersam, N. P. Guisinger, *Nat. Rev. Chem.* **2017**, *1*, 0014.
[5] L. Li, Y. Yu, G. J. Ye, Q. Ge, X. Ou, H. Wu, D. Feng, X. H. Chen, Y. Zhang, *Nat. Nanotech.* **2014**, *9*, 372.
[6] F. Ersan, D. Kecik, V. O. Özçelik, Y. Kadioglu, O. Ü. Aktürk, E. Durgun, E. Aktürk, S. Ciraci, *Appl. Phys. Rev.* **2019**, *6*, 021308.
[7] S. Mohsen Beladi-Mousavi, M. Pumera, *Chem. Soc. Rev.* **2018**, *47*, 6964.
[8] V. Lloret, M. Á. Rivero-Crespo, J. A. Vidal-Moya, S. Wild, A. Doménech-Carbó, B. S. J. Heller, S. Shin, H.-P. Steinrück, F. Maier, F. Hauke, M. Varela, A. Hirsch, A. Leyva-Pérez, G. Abellán, *Nat. Commun.* **2019**, *10*, 509.

[9] P. Kumar Roy, J. Luxa, Z. Sofer, *Nanoscale* **2020**, *12*, 10430.
[10] W. Tao, N. Kong, X. Ji, Y. Zhang, A. Sharma, J. Ouyang, B. Qi, J. Wang, N. Xie, C. Kang, H. Zhang, O. C. Farokhzad, J. S. Kim, *Chem. Soc. Rev.* **2019**, *48*, 2891.
[11] M. A. Lucherelli, V. Oestreicher, M. Alcaraz, G. Abellán, *Chem. Commun.* **2023**, *59*, 6453.
[12] S. Zhang, W. Zhou, Y. Ma, J. Ji, B. Cai, S. A. Yang, Z. Zhu, Z. Chen, H. Zeng, *Nano Lett.* **2017**, *17*, 3434.
[13] S. Zhang, Z. Yan, Y. Li, Z. Chen, H. Zeng, *Angew. Chem.* **2015**, *127*, 3155.
[14] J. A. Carrasco, P. Congost-Escoin, M. Assebban, G. Abellán, *Chem. Soc. Rev.* **2023**, *52*, 1288.
[15] C. Gibaja, D. Rodriguez-San-Miguel, P. Ares, J. Gómez-Herrero, M. Varela, R. Gillen, J. Maultzsch, F. Hauke, A. Hirsch, G. Abellán, F. Zamora, *Angew. Chem.* **2016**, *128*, 14557.
[16] C. Gibaja, M. Assebban, I. Torres, M. Fickert, R. Sanchis-Gual, I. Brotons, W. S. Paz, J. José Palacios, E. G. Michel, G. Abellán, F. Zamora, *J. Mater. Chem. A* **2019**, *7*, 22475.
[17] N. Antonatos, H. Ghodrati, Z. Sofer, *Appl. Mater. Today* **2020**, *18*, 100502.
[18] X. Wu, Y. Shao, H. Liu, Z. Feng, Y.-L. Wang, J.-T. Sun, C. Liu, J.-O. Wang, Z.-L. Liu, S.-Y. Zhu, Y.-Q. Wang, S.-X. Du, Y.-G. Shi, K. Ibrahim, H.-J. Gao, *Adv. Mater.* **2017**, *29*, 1605407.
[19] J. Ji, X. Song, J. Liu, Z. Yan, C. Huo, S. Zhang, M. Su, L. Liao, W. Wang, Z. Ni, Y. Hao, H. Zeng, *Nat. Commun.* **2016**, *7*, 13352.
[20] I. Torres, M. Alcaraz, R. Sanchis-Gual, J. A. Carrasco, M. Fickert, M. Assebban, C. Gibaja, C. Dolle, D. A. Aldave, C. Gómez-Navarro, E. Salagre, E. García Michel, M. Varela, J. Gómez-Herrero, G. Abellán, F. Zamora, *Adv. Funct. Mater.* **2021**, *31*, 2101616.
[21] S. Wolff, R. Gillen, M. Assebban, G. Abellán, J. Maultzsch, *Phys. Rev. Lett.* **2020**, *124*, 126101.
[22] M. Assebban, C. Gibaja, M. Fickert, I. Torres, E. Weinreich, S. Wolff, R. Gillen, J. Maultzsch, M. Varela, S. Tan Jun Rong, K. P. Loh, E. G. Michel, F. Zamora, G. Abellán, *2D Mater.* **2020**, *7*, 025039.
[23] M. Fickert, M. Assebban, J. Canet-Ferrer, G. Abellán, *2D Mater.* **2020**, *8*, 015018.
[24] P. S. Kollipara, J. Li, Y. Zheng, *Research* **2020**, *2020*, 6581250.
[25] C. Dolle, V. Oestreicher, A. M. Ruiz, M. Kohring, F. Garnes-Portolés, M. Wu, G. Sánchez-Santolino, A. Seijas-Da Silva, M. Alcaraz, Y. M. Eggeler, E. Spiecker, J. Canet-Ferrer, A. Leyva-Pérez, H. B. Weber, M. Varela, J. J. Baldoví, G. Abellán, *J. Am. Chem. Soc.* **2023**, *145*, 12487.
[26] L. Peng, S. Ye, J. Song, J. Qu, *Angew. Chem.* **2019**, *131*, 9996.
[27] G. He, T. Dong, Z. Yang, P. Ohlckers, *Chem. Mater.* **2019**, *31*, 9917.
[28] A. E. Rezaee, M. Almasi Kashi, A. Baktash, *Mater. Sci. Eng., B* **2018**, *236–237*, 208.
[29] J. Gaberle, A. L. Shluger, *Nanoscale* **2018**, *10*, 19536.
[30] M. Xie, S. Zhang, B. Cai, Y. Gu, X. Liu, E. Kan, H. Zeng, *Nano Energy* **2017**, *38*, 561.
[31] Q.-T. Zhang, Y.-T. Tseng, K.-C. Lu, C.-W. Huang, H.-F. Hsu, W.-W. Wu, *Scr. Mater.* **2023**, *226*, 115262.
[32] M. Balkanski, R. F. Wallis, E. Haro, *Phys. Rev. B* **1983**, *28*, 1928.
[33] A. S. Pawbake, M. S. Pawar, S. R. Jadkar, D. J. Late, *Nanoscale* **2016**, *8*, 3008.
[34] I. Calizo, A. A. Balandin, W. Bao, F. Miao, C. N. Lau, *Nano Lett.* **2007**, *7*, 2645.
[35] P. Ares, F. Aguilar-Galindo, D. Rodríguez-San-Miguel, D. A. Aldave, S. Díaz-Tendero, M. Alcamí, F. Martín, J. Gómez-Herrero, F. Zamora, *Adv. Mater.* **2016**, *28*, 6332.
[36] Q. Wu, Y. J. Song, *Chem. Commun.* **2018**, *54*, 9671.
[37] S. Wild, V. Lloret, V. Vega-Mayoral, D. Vella, E. Nuin, M. Siebert, M. Koleśnik-Gray, M. Löffler, K. J. J. Mayrhofer, C. Gadermaier, V. Krstić, F. Hauke, G. Abellán, A. Hirsch, *RSC Adv.* **2019**, *9*, 3570.
[38] Z. Zafar, Z. H. Ni, X. Wu, Z. X. Shi, H. Y. Nan, J. Bai, L. T. Sun, *Carbon* **2013**, *61*, 57.
[39] S. J. Kim, S. J. Park, H. Y. Kim, G. S. Jang, D. J. Park, J.-Y. Park, S. Lee, Y. H. Ahn, *Appl. Phys. Lett.* **2016**, *108*, 203111.
[40] N. S. Mueller, S. Heeg, M. P. Alvarez, P. Kusch, S. Wasserroth, N. Clark, F. Schedin, J. Parthenios, K. Papagelis, C. Galiotis, M. Kalbáč, A. Vijayaraghavan, U. Huebner, R. Gorbachev, O. Frank, S. Reich, *2D Mater.* **2017**, *5*, 015016.